Dispersion enhancement and damping by buoyancy driven flows in two-dimensional networks of capillaries

Maria Veronica D'Angelo,[1,2,a)] Harold Auradou,[1,b)] Catherine Allain,[1] Marta Rosen,[2] and Jean-Pierre Hulin[1,c)]
[1]*Université Pierre et Marie Curie-Paris 6, Université Paris-Sud, CNRS and Laboratoire FAST, Batiment 502, Campus Universitaire, Orsay F-91405, France*
[2]*Grupo de Medios Porosos, Facultad de Ingenieria, Paseo Colon 850, 1063 Buenos Aires, Argentina*

(Received 27 September 2007; accepted 29 February 2008; published online 31 March 2008)

The influence of a small relative density difference ($\Delta\rho/\rho \simeq 3\times10^{-4}$) on the displacement of two miscible Newtonian liquids is studied experimentally in transparent two-dimensional square networks of microchannels held vertically; the channel width distribution is log normal with a mean value of $a=0.33$ mm. Maps of the local relative concentration are obtained by an optical light absorption technique. Both stable displacements in which the denser fluid enters at the bottom of the cell and displaces the lighter one and unstable displacements in which the lighter fluid is injected at the bottom and displaces the denser one are realized. Except at the lowest mean flow velocity U, the average $C(x,t)$ of the relative concentration satisfies a convection-dispersion equation. The relative magnitude of $|U|$ and of the velocity U_g of buoyancy driven fluid motions is characterized by the gravity number $N_g=U_g/|U|$. At low gravity numbers $|N_g|<0.01$ (or equivalently high Péclet numbers $\mathrm{Pe}=Ua/D_m>500$), the dispersivities l_d in the stable and unstable configurations are similar to $l_d \propto \mathrm{Pe}^{0.5}$. At low velocities such that $|N_g|>0.01$, l_d increases like 1/Pe in the unstable configuration ($N_g<0$), while it becomes constant and close to the length of individual channels in the stable case ($N_g>0$). Isoconcentration lines $c(x,y,t)=0.5$ are globally flat in the stable configuration, while in the unstable case, they display spikes and troughs with a rms amplitude σ_f parallel to the flow. For $N_g>-0.2$, σ_f increases initially with the distance and reaches a constant limit, while it keeps increasing for $N_g<-0.2$. A model taking into account buoyancy forces driving the instability and the transverse exchange of tracer between rising fingers and the surrounding fluid is suggested and its applicability to previous results obtained in three-dimensional media is discussed. © *2008 American Institute of Physics*. [DOI: 10.1063/1.2899635]

I. INTRODUCTION

Miscible displacements in porous media are encountered in many environmental, water supply and industrial problems.[1–3] Specific types of miscible displacements, such as tracer dispersion, are also usable as diagnostic tools to investigate porous media heterogeneities at the laboratory[4] or field scales. The characteristics of these processes, such as the width and the geometry of the displacement front, are often influenced by contrasts between the properties of the displacing and displaced fluids such as their density.[5–8] When the fluid density increases with height, gravity driven instabilities may appear and broaden the displacement front: As an unwanted result, this may lead to early breakthroughs of the displacing fluid. An example is the infiltration of a dense plume of pollutant into a saturated medium.

The objective of the present paper is to study experimentally at both the local and global scales miscible displacements of two fluids of slightly different densities ($\Delta\rho/\rho \simeq 3\times10^{-4}$): Of particular interest is the influence of buoyancy driven flow perturbations on the structure and development of the mixing zone.

In porous media, from Darcy's law, the flow per unit area, U_g (counted positively for upward flow), induced by the difference between the hydrostatic pressure gradients in the two fluids is

$$U_g = -k\frac{\Delta\rho g}{\mu}, \tag{1}$$

in which $\Delta\rho$ is the density of the lower fluid minus that of the upper one, μ is the viscosity (identical for both fluids), and k is the permeability of the medium. The relative magnitude of U_g and of the mean flow velocity U is a key element of the problem and is characterized by the gravity number:[8]

$$N_g = -\frac{U_g}{|U|} = \frac{\Delta\rho g k}{\mu|U|}. \tag{2}$$

With the above definition of $\Delta\rho$, one has $N_g>0$ in the stable configuration (denser fluid below the lighter one) and $N_g<0$ in the unstable one.

Recent experiments[5–7] have shown that, even when the parameter $|N_g|$ is small (2×10^{-2} in Ref. 5), the geometry of the mixing fronts is still influenced by buoyancy. Variable

a)Electronic mail: vdangelo@fi.uba.ar.
b)Electronic mail: auradou@fast.u-psud.fr.
c)Electronic mail: hulin@fast.u-psud.fr.

density flow and transport in porous media has therefore received increasing attention both theoretically and numerically.[9–11]

In the present work, miscible displacements of fluids of slightly different densities are studied optically in a transparent two-dimensional (2D) vertical network of channels with random widths.[12] Both visualizations at the pore scale (one of the fluids is dyed) and measurements of the global concentration profiles parallel to the mean flow at different mean velocities U are achieved. The development and influence of buoyancy driven flows are analyzed by comparing displacement processes in stable and unstable density contrast configurations.

For density contrasts low enough so that $|N_g| \leqslant 0.2$, hydrodynamic dispersion damps the development of instabilities. Then the mixing process can be considered as dispersive and is described well by the macroscopic convection-dispersion equation classically used for passive tracers with

$$\frac{\partial C}{\partial t} = \vec{\nabla} \cdot (\vec{U} \cdot C - \bar{D} \cdot \vec{\nabla} C), \tag{3}$$

where C is the tracer concentration, $\vec{U}$ is the flow velocity, and $\bar{D}$ is the dispersion tensor (all values are averaged over the gap of the cell); $\bar{D}$ is assumed to reduce to the diagonal components $D_{\parallel}$ and $D_{\perp}$ corresponding to directions parallel and perpendicular, respectively, to the mean flow. The values of $D_{\parallel}$ and $D_{\perp}$ are determined by two main physical mechanisms: advection by the velocity field inside the medium and molecular diffusion (characterized by a molecular diffusion coefficient D_m). The relative magnitude of these two effects is characterized by the Péclet number $\mathrm{Pe} = Ua/D_m$ (a here is the average channel width).

Both immiscible displacements[12] and tracer dispersion[4,13] have already been measured previously in such models. This latter work[13] uses the same experimental technique and porous model as the present ones but deals with experimental conditions in which the development of buoyancy driven instabilities is negligible. In this case, the dye can be considered as an "ideal" tracer that does not modify the fluid properties. In contrast, the present work deals with the influence of buoyancy effects on dispersion: The components of $\bar{D}$ depend on $\Delta\rho$ and are larger in the unstable configuration. Similar studies might be performed on three-dimensional (3D) porous samples using NMR imaging, computed tomography imaging scan, acoustical techniques,[14,15] or positron emission projection imaging[16] but at a higher cost and/or with strong constraints on the fluid pairs to be used.

In the present displacement experiments, concentration maps obtained for a vertical flow are compared for different flow velocities. At the global scale, an effective dispersion coefficient is determined and its dependence on the flow velocity is studied in both stable and unstable density contrast configurations. At the local scale, the variation of geometrical front features of different sizes is analyzed as a function of the flow velocity and of time. The combination of these local and global data provides both a sensitive detection of the instabilities and information on the characteristics of the displacement process at different length scales. Finally, a model aimed at interpreting semiquantitatively these results and also previous observations on 3D systems is presented.

II. DESCRIPTION OF EXPERIMENT

A. Experimental setup and procedure

The experimental system and the technique for analyzing the data have already been described in Ref. 13. The model medium is a vertical transparent 2D square network of channels of random aperture:[12] It has a mesh size equal to $d=1$ mm and contains 140×140 channels with a mean length of 0.67 mm and a depth of 0.5 mm. The width of the channels takes seven values between 0.1 and 0.6 mm with a log-normal distribution and a mean value of $a=0.33$ mm. The permeability of the network is $k=3 \times 10^{-9}$ m^2 (i.e., 3000 Darcy).

The model is vertical with its open sides horizontal (see Fig. 2 in Ref. 13). The upper side is connected to a syringe pump sucking the fluids upward out of the model from a reservoir inside which the lower side is dipped. Initially, the model is saturated by pumping the first fluid of density ρ_1 out of the lower reservoir into the model. Then, the pump is switched off and the lower side of the model is removed from the liquid bath by lowering the reservoir (the connection tubes are shut to avoid unwanted fluid exchange between the model and the outside during this process). The reservoir is then emptied completely, filled up by the second fluid of density $\rho_2 = \rho_1 + \Delta\rho$, and raised again until the lower side of the model is below the liquid surface. The displacement process is initiated by opening the connection tubes and switching on the pump. This procedure provides a perfectly straight initial front between the two fluids at the beginning of the displacement. The mean flow velocity ranges from 0.005 to 2.5 mm s^{-1}.

B. Fluid characteristics

Newtonian water-glycerol mixtures obtained by mixing 60% in weight of glycerol in pure water are used in the experiments. Their viscosity is equal to $\mu = 10^{-2}$ Pa s at 20 °C. The injected and displaced fluids are identical but for water blue dye[17] added to one of the solutions, allowing one both to measure the local concentration optically and to introduce a controllable density difference between the fluids (note that since the density contrast is purely due to the dye, the optical determination of the local dye concentration also measures the local density).

In this work, the absolute value $|\Delta\rho|$ of the density difference between the two fluids is constant with $|\Delta\rho| = 0.3$ kg/m^3. For each flow rate and pair of fluids used, both stable ($\Delta\rho > 0$) and unstable ($\Delta\rho < 0$) configurations are studied by swapping fluids 1 and 2.

Water blue dye has been selected because it provides a large optical absorption for a minimal amount of dye and does not get adsorbed on the walls of the flow channels. Its molecular diffusion coefficient in water

is $D_m = 6.5 \times 10^{-4}$ mm^2 s^{-1} and, therefore, $D_m^* = 0.7 \times 10^{-4}$ mm^2 s^{-1} in the water-glycerol solutions (assuming $D_m \propto \mu^{-1}$).

The model is illuminated from the back by a light panel and images are acquired by a 12 bit high stability digital camera with a 1040×1400 pixel resolution (pixel size $=0.16$ mm). Typically, 100 images are recorded for each experiment at time intervals between 2.5 and 700 s. The images are translated into maps of the relative concentration $C(x,y,t)$ of the fluids using a calibration procedure commonly used[7] and described in Refs. 13 and 18.

C. Characteristic parameters of buoyant flows

In the present experiments, the modulus $|U_g|$ of the buoyant flow velocity [see Eq. (1)] is constant (only its sign changes when the fluids are swapped): The gravity number N_g varies then as U^{-1} with the velocity, and the influence of gravity is largest at the lowest velocities. Using Eq. (1) in order to estimate U_g for the water-glycerol mixtures used in the present work leads to $|U_g| = 10^{-3}$ mm s^{-1} for the glycerol-water mixture. At the lowest experimental flow velocity ($U = 5 \times 10^{-3}$ mm s^{-1}), the duration of the complete saturation of the network is $t \simeq 3 \times 10^4$ s. During this time lapse, the distance $U_g t$ characterizing the growth of the gravitational instabilities is 28 mm for the water-glycerol mixture: This is far above the length d of the individual channels of the network, and a noticeable influence of gravity on the structure of the displacement fronts is thus expected.

For these same solutions, buoyancy effects should be sizable when the distance $U_g t$ becomes larger than d: The transition should then take place at an imposed flow velocity $U_c = U_g L/d \simeq 0.14$ mm s^{-1} (L is the model length). This velocity corresponds to the following gravity and Péclet numbers: $N_g^c \simeq -0.01$ and $\mathrm{Pe}^c \simeq 500$. These predictions will be shown in Sec. III C to correspond well to the experimental results.

III. EXPERIMENTAL RESULTS

A. Qualitative observations of miscible displacements

Figure 1 displays concentration distributions observed during displacement experiments using the water-glycerol mixture. In the stable configuration of Figs. 1(d)–1(f), the mean global front shape remains flat at all flow velocities. The overall width of the mixing zone increases, however, with the flow rate due to the development of fine structures parallel to the mean flow, particularly at the highest velocity [Fig. 1(f)].

In the unstable configuration and at the lowest velocity [Fig. 1(a)], large instability fingers with a width of the order of 10–15 mesh sizes appear and grow up to a length equal to that of the experimental model. For a velocity four times higher, fingers still appear but they are significantly shorter [Fig. 1(b)]. As the velocity increases, the size of the fingers parallel to the mean flow decreases, while finer features develop. For a velocity 50 times higher [Fig. 1(c)], the front geometry is then more similar to that observed in the stable case although its width parallel to the flow is still broader. In Sec. III E, the structure of the mixing zone in these experiments will be analyzed again in the unstable case from the geometry of the isoconcentration fronts $[C(x,y,t) = 0.5]$.

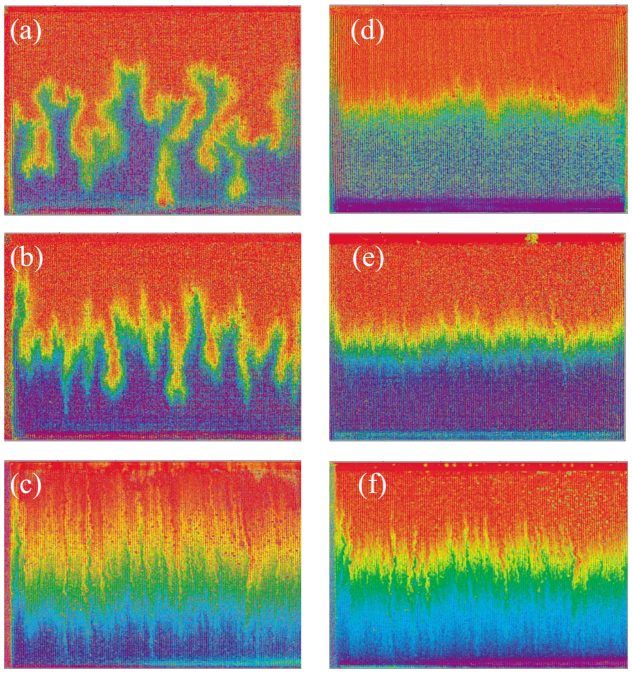

FIG. 1. (Color online) Relative concentration maps for experiments using water-glycerol solutions of different densities at three different flow rates with the injected fluid occupying half of the model. [(a) and (d)] $U = 0.005$ mm s^{-1}, $|N_g| = 0.2$; [(b) and (e)] $U = 0.025$ mm s^{-1}, $|N_g| = 0.04$; [(c) and (f)] $U = 1.25$ mm s^{-1}, $|N_g| = 8 \times 10^{-4}$. Experiments correspond to stable [(d)–(f)] and unstable [(a)–(c)] density contrast configurations. In these figures and the following ones, darker shades correspond to the pure injected or displaced fluid and the lighter shade to a mixture of the two (in the online version, purple and red colors correspond, respectively, to the injected and displaced fluids and other colors to a mixture). Fluid flows are upward with $\vec{g}$ pointing downward. Field of view is 153×140 mm^2 in the vertical and horizontal directions (images are stretched horizontally).

These results agree qualitatively with macroscopic dispersion measurements on 3D bead packs[5] using conductivity tracers detected at the outlet of the samples. In this case, buoyancy driven instabilities are also observed at low velocities for Newtonian water-glycerol solutions in a gravitationally unstable configuration but not for water-scleroglucan solutions. Compared to this latter work, optical measurements provide additional information on front structures of different sizes. We now examine the variation of the global dispersion characteristics as a function of the experimental parameters and of the configuration of the fluids.

B. Quantitative concentration variation analysis

The procedure for determining a global dispersion coefficient from the concentration maps is described in detail in Ref. 13. The mean relative concentration $C(x,t)$ of a heavy (dyed) fluid at a distance x from the inlet side is first determined by averaging the value $c(x,y,t)$ for individual pixels over a window of width $\Delta y = 140$ mm across the flow (only pixels belonging to the pore volume are included in the average). Figures 2(a) and 2(b) display the variations with time of $C(x,t)$ for two different values of the gravity number N_g.

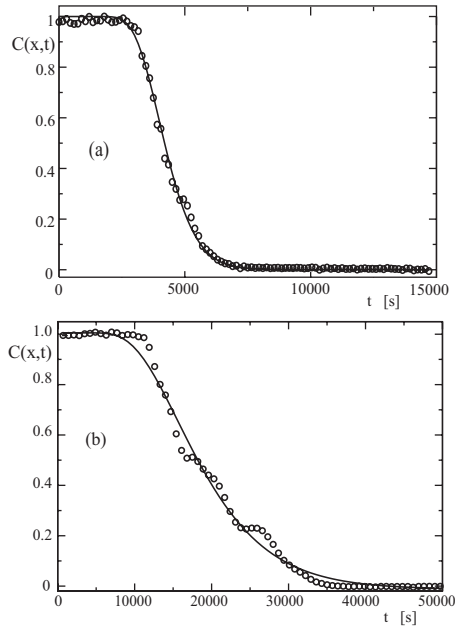

FIG. 2. Normalized mean concentration variation $C(x,t)$ as a function of the time t for unstable displacement experiments using a water-glycerol mixture [C: Average of local pixel concentration $c(x,y,t)$ over a width $\Delta y \simeq 140$ mm in the central part of the model]. (a) $U=0.025$ mm s^{-1}, $N_g=-0.04$, $x=104$ mm. (b) $U=0.005$ mm s^{-1}, $N_g=-0.2$, $x=88$ mm. Continuous line: Fit by a solution of Eq. (3) with (a) $\bar{t}=4350$ s, $D_\parallel/U^2=110$ s and (b) $\bar{t}=18\,266$ s, $D_\parallel/U^2=1369$ s. The determination of the mean velocity U is discussed in Sec. III B.

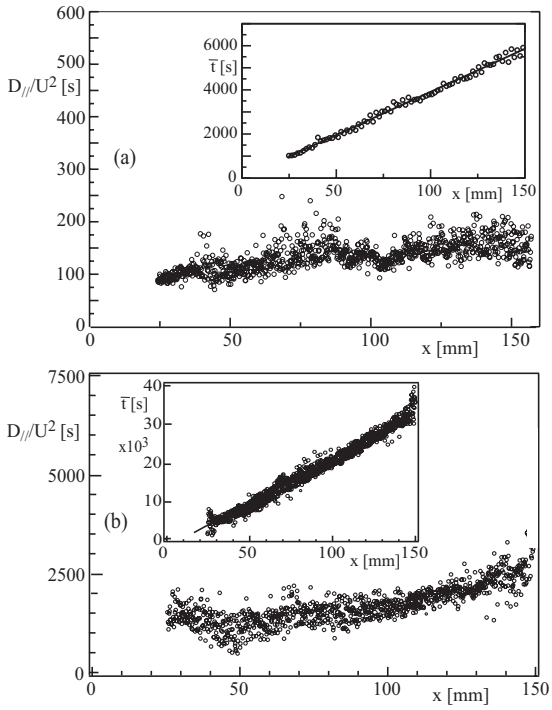

FIG. 3. Variation of the fitting parameter $D_\parallel/U^2$ as a function of the distance x from the inlet for two unstable displacement experiments using the water-glycerol solutions with $U=0.025$ mm s^{-1} ($N_g=-0.04$) and $U=0.005$ mm s^{-1} ($N_g=-0.2$). Insets: Variation of the mean transit time $\bar{t}$ as a function of x. Solid line: Linear regression of the data. Values of $\bar{t}$ and $D_\parallel/U^2$ are obtained by fitting the mean concentration variation $C(x,t)$ using Eq. (3) at each distance x.

These variations have been fitted (continuous line) by the following one-dimensional solution of the convection diffusion equation (3) assuming an initial steplike variation of C at the inlet:

$$C(x,t)=\frac{1}{2}\left[1+\frac{N_g}{|N_g|}\,\mathrm{erf}\left(\frac{t-\bar{t}}{\sqrt{4D_\parallel t/U^2}}\right)\right]. \tag{4}$$

Here, $D_\parallel$ is equal to the diagonal component of the tensor D in the x direction. Since flow is always upward, adding the factor $N_g/|N_g|=\pm 1$ makes the equation usable both for light fluid displacing heavy fluid (unstable configuration, $N_g<0$) and for heavy fluid displacing light fluid (stable configuration, $N_g>0$).

For $N_g=-0.04$, the experimental data are well fitted by Eq. (4). For $N_g=-0.2$, the distortions of the front due to the instabilities are very large and the concentration does not decrease smoothly but the experimental curve displays bumps; these features are the signature of rising fingers reaching the measurement height. Yet, an acceptable fit of the experimental data with Eq. (4) can still be achieved. The fits provide the values of the mean transit time $\bar{t}$ of the front at the distance x and of the ratio $D_\parallel/U^2=\bar{\Delta}t^2/(2\bar{t})$ ($\bar{\Delta}t^2$ is the centered second moment of the transit times along the distance x).

The insets of Figs. 3(a) and 3(b) display the variation of $\bar{t}$ with the distance x which is linear in both cases; this shows that the mixing zone characterized by the mean concentration profile $C(x,t)$ moves at a constant velocity U_{mz} equal to the inverse of the slope of the variation. A linear regression of the data provides the values $U_{mz}=0.027$ mm s^{-1} for case (a) and $U_{mz}=0.0046$ mm s^{-1} for case (b). The mean fluid velocity U in the model may be taken to be equal to the ratio of the injected flow rate and of the pore volume per unit length along x which have been determined independently. The values of U computed in this way at the same two flow rates as above are $U=0.025$ and 0.005 mm s^{-1}, respectively: They are very close to the corresponding values of U_{mz}.

The two velocities U and U_{mz} are compared more precisely in Fig. 4, which displays the values of U_{mz}/U for both stable (○) and unstable (●) flow configurations. This ratio is always close to 1: This shows that buoyancy effects do not influence the mean displacement of the concentration profile even at the lowest flow rate ($N_g=-0.2$) for which they are very large [Fig. 1(a)]. One assumes therefore in the following that $U=U_{mz}$.

The main graphics of Figs. 3(a) and 3(b) display the variation of the ratio $D_\parallel/U^2$ as a function of the distance x from the inlet. In case (a) ($N_g=-0.04$), $D_\parallel/U^2$ increases slightly at first with the distance x and levels off for $x\geqslant 50$ mm; then it fluctuates around a constant value. Previous studies[13] have shown that the fluctuations are periodic and determined by the structure of the network (the period is equal to the mesh size). In case (b) ($N_g=-0.2$), $D_\parallel/U^2$ fluctuates around a constant value for $x\leqslant 100$ mm and increases slightly with x at larger distances. This is likely due to the rising fingers, directly observable in Fig. 1(a) and which can be identified on the curve of Fig. 2(b). Tracers are advected

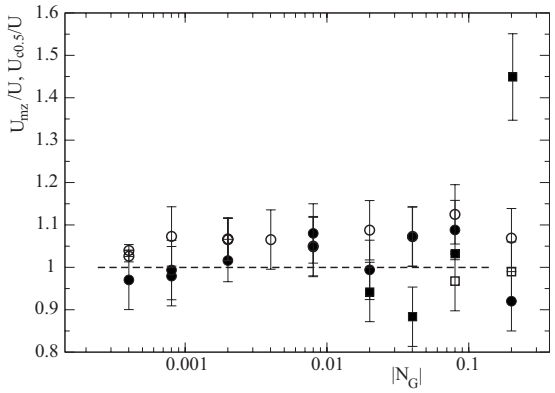

FIG. 4. Variation as a function of $|N_g|$ of the characteristic velocities of the fluid displacement normalized by the mean velocity U in stable (open symbols) and unstable (dark symbols) density contrast configurations for water-glycerol solutions. [(○) and (●)] Normalized velocity of the mixing region U_{mz}/U determined by a linear regression on the variation of $\bar{t}$ as a function of x [see insets of Figs. 3(a) and 3(b)]. (□ and ■) $U_{c0.5}$=mean velocity of isoconcentration lines $c=0.5$.

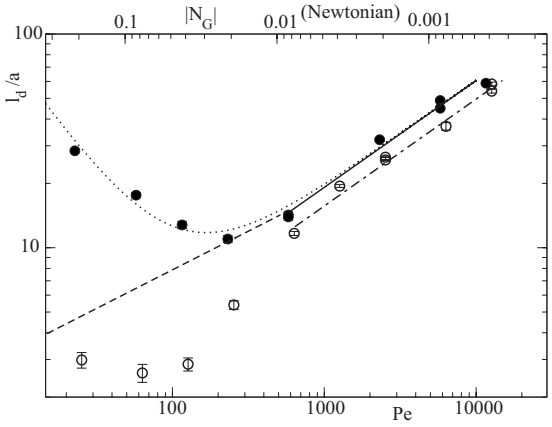

FIG. 5. Variation of the dispersivity $l_d/a=D/aU$ as a function of the Péclet number Pe and of the gravity parameter N_g (upper axis) for the water-glycerol mixture for $N_g>0$ (○) and $N_g<0$ (●). Solid ($l_d/a=0.6\ \mathrm{Pe}^{0.5}$) and dash-dotted ($l_d/a=0.5\ \mathrm{Pe}^{0.5}$) lines: Regression for water-glycerol data for the stable and unstable configurations, respectively, in the buoyancy-free flow domain ($-0.01<N_g<0.01$). Dotted line: Variation predicted by Eq. (9) (see Sec. IV) for $\beta_T=0$ and $\epsilon=0.3$). Dashed line: Variation law $l_d/a=1.5\ \mathrm{Pe}^{0.35}$ satisfied from Ref. 13 by data corresponding to shear-thinning polymer solutions.

faster and farther inside these fingers than outside, resulting in an increase of the dispersivity. Even in this case, however, the fluctuations of the measurements and the relatively small variations of the values of $D_\parallel/U^2$ do not allow one to conclude that a diffusive regime is not reached.

These results show both that the mixing front moves at a constant velocity U and that (except perhaps for $N_g=-0.2$) it reaches a dispersive spreading regime characterized by a dispersion coefficient $\langle D_\parallel \rangle$ taken to be equal to the average of $D_\parallel$ over the full experimental range of x values. In the following, like in Ref. 13, dispersion is characterized by the dispersivity $l_d=\langle D_\parallel \rangle/U$ instead of $\langle D_\parallel \rangle$; the standard deviation of the individual values of $D_\parallel$ is used to estimate the error bars on l_d.

C. Global dispersion measurement results

We now discuss the variations of the normalized dispersivity l_d/a in the stable and unstable configurations: l_d/a is plotted in Fig. 5 as a function of the Péclet number $\mathrm{Pe}=Ua/D_m$ (bottom axis) and the gravity number $|N_g|$ (top axis) for the water-glycerol solution. Data points corresponding to $N_g<0$ and $N_g>0$ are clearly separated at high $|N_g|$ (or equivalently low Pe) values: This separation occurs close to the transition value $N_g^c=0.01$ (or $\mathrm{Pe}^c=500$) discussed in Sec. II C. Experiments on 3D bead packings[5] displaying a similar effect are compared to the present ones in Sec. IV. This separation reflects the development of fingerlike structures at low velocities in the unstable configuration ($N_g<0$) and the flattening of the front in the stable one ($N_g>0$) displayed in Fig. 1. At the lowest Péclet number, the values of l_d for $N_g>0$ and $N_g<0$ differ by a factor of nearly 10.

For $N_g>0$, the dispersivity l_d reaches for $N_g\simeq 5\times 10^{-2}$ ($\mathrm{Pe}\simeq 100$) a minimum value $l_d\simeq 1$ mm close to the characteristic local length, i.e., the mesh size of the lattice. In homogeneous porous media, this length often represents a lower limit of l_d for a perfectly passive tracer: This low value confirms the stabilizing influence of the buoyancy forces.[8]

At velocities U above 0.1 mm s^{-1} (or $\mathrm{Pe}>500$), l_d is similar for both $N_g>0$ and <0 and increases as $l_d\propto \mathrm{Pe}^\alpha$ with $\alpha\simeq 0.5$ (solid and dash-dotted lines in Fig. 5). This variation differs from the slow increase observed in 3D media such as homogeneous grain packings:[5] It reflects the combined effects of geometrical dispersion due to the disorder of the velocity field and of Taylor dispersion due to the velocity profiles in individual channels. The latter becomes important at high Péclet numbers due to the reduced mixing at the junctions by transverse molecular diffusion. As a result, the correlation length of the velocity of the tracer particles along their trajectories (and therefore the dispersivity l_d) becomes larger.

The above analysis of the global dispersion has used averages of the local concentration over nearly the full width of the model and including all the geometrical features of the front instabilities. The corresponding value of l_d then combines different types of effects.

The first one is the local spreading of the displacement front. It is likely to result from the combined effects of the local disorder of the flow field (geometrical dispersion mechanism) and the flow profile between the rough walls (Taylor mechanisms). The influence of these mechanisms is discussed in Ref. 13.

The second more global effect is the global spreading of the mixing zone due to fluid velocity contrasts between different flow paths (resulting, for instance, from the instabilities). This will be studied in Sec. III E specifically from the variations of the front geometry.

D. Comparison with dispersion measurements on the same models using high viscosity polymer solutions

It is informative to apply the above approaches to measurements previously reported on the same experimental systems using water-sleroglucan solutions of concentrations C_p=500 ppm and C_p=1000 ppm.[13] In this case, no buoyancy induced instability occurred in the unstable configurations even at velocities equal to the lowest ones in the present work. This results from the very high effective viscosity μ of these solutions at low shear rates for which instabilities are most likely to develop. μ is independent of the shear rate $\dot{\gamma}$ below a transition value $\dot{\gamma}_0$ of the orders of 0.08 and 0.025 s^{-1}, respectively, for the 500 and 1000 ppm solutions. In this "Newtonian plateau" domain, the corresponding viscosities μ_0 are 410 and 4500 mPa s.

Using the same method as in Sec. II C, an upper limit of the value of N_g can be therefore estimated by taking $\mu=\mu_0$ in Eq. (2) at the lowest experimental flow velocity (in this case, one has $\dot{\gamma}<\dot{\gamma}_0$ for both solutions). This gives $|N_g|=5\times10^{-3}$ and $|N_g|=4.5\times10^{-4}$, respectively, for the 500 and 1000 ppm solutions. Both values are below the threshold of the instabilities observed for the Newtonian fluids, in agreement with the experimental observations.

As could be expected from these results, the values of l_d are also the same for the stable and unstable configurations for these polymer solutions: l_d increases with Pe following a power law $l_d \propto \mathrm{Pe}^{\alpha}$ (dashed line in Fig. 5). This variation is similar to that satisfied at high Pe values by the water-glycerol solutions but the value of α is lower ($\alpha \simeq 0.35$ instead of 0.5). This difference may be due to the different relative weights of the Taylor and geometrical mechanisms for these two types of fluids (see Refs. 13 and 18) These solutions display indeed shear-thinning properties at high flow rates (while they behave like Newtonian fluids at low ones): This reduces Taylor dispersion and enhances geometrical dispersion compared to the Newtonian case.

E. Spatial structure of the displacement fronts for unstable flows

Previous experiments in 3D porous media[15] demonstrated a clear amplification of front structures resulting from permeability heterogeneities for gravitationally unstable displacements. Such effects can be studied precisely here down to small length scales, thanks to the 2D geometry of the model network and to the high precision and spatial resolution of the optical concentration measurements.

In the following, the front geometry is characterized from the lines $x_f(y,t)$ along which the local relative concentration $c(x,y,t)$ is equal to 0.5 at a given time t. Examples of such lines determined by a thresholding procedure at four gravity numbers $-0.2 \leqslant N_g \leqslant -0.001$ are displayed in Fig. 6.

At the lowest flow velocity investigated ($N_g=-0.2$, $\mathrm{Pe} \simeq 25$), the buoyancy driven flow components have a major influence on the front geometry and several instability fingers soar up while the front displacement is much slower in other regions [Fig. 6(d)].

At higher mean flow velocities [Figs. 6(b) and 6(c)], the front retains a rough geometry, still reflecting buoyancy driven flow components but its mean advancing motion is clearly visible. In contrast, for $N_g=-0.2$ [Fig. 6(d)], the development of the front appears as the combination of the independent growth of the individual fingers.

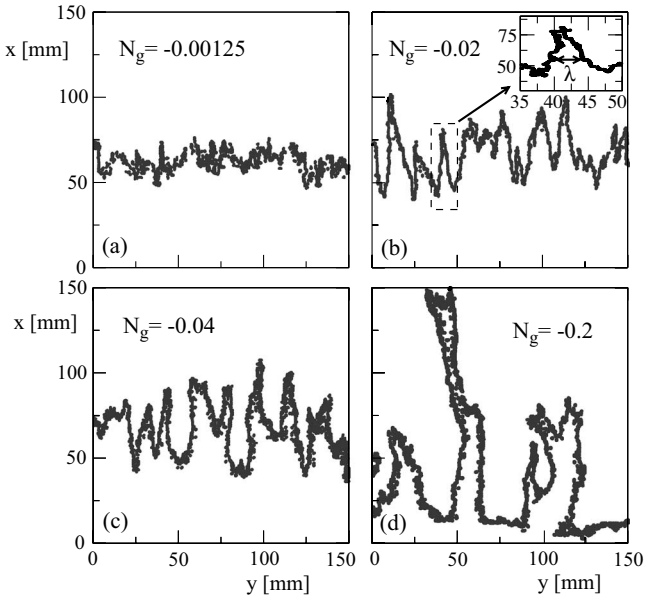

FIG. 6. Isoconcentration fronts $x_f(y,t)$ measured at four different gravity numbers N_g=(a) −0.001 25, (b) −0.02, (c) −0.04, and (d) −0.2 for water-glycerol mixtures in an unstable flow configuration (the injected fluid occupies half of the model area). Flow is upward with $\vec{g}$ oriented downward. The inset in (b) displays the typical size of the spikes λ.

Another important feature is the fact that the distance y across the front at which corresponding geometrical features (peaks and troughs) appear remains the same. For $N_g=-0.2$, the extension of these features parallel to the flow increases and they cluster together into larger structures, as can be seen by comparing Fig. 6(a) and Figs. 6(b) and 6(c). Moreover, for $-0.2<N_g\leqslant-0.02$, and even though the width of the front parallel to the mean flow increases significantly, the typical transverse size λ (along y) of the individual spikes of the front is fairly constant with $\lambda \simeq 4-5$ mm. This value has been taken to be equal to the mean interval (along y) between successive local maxima of the local distance (parallel to x) of the front from the inlet side [see inset on Fig. 6(b)].

These results contrast with the assumptions of a varying wavelength[7] often applied to porous media following observations in Hele-Shaw cells.[19] However, for the latter, there is no characteristic length scale for the flow field in the cell beyond its thickness; in the present case, on the contrary, the location of the features of the front are determined by the heterogeneities of the flow field. At still higher flow velocities [for instance, in Fig. 6(a)] and for $N_g>N_g^c=-0.01$ (see Sec. II C for the expression of N_g^c), distortions of the front due to buoyancy effects decrease in size and become hardly visible on the isoconcentration lines.

Quantitatively, we characterize the isoconcentration fronts by their mean position along the flow $\overline{x_f(t)}=\langle x_f(y,t)\rangle_y$ and by the rms fluctuations σ_f of the distance $x_f(y,t)$ [$\sigma_f=(\langle[x_f(y,t)-\overline{x_f(t)}]^2\rangle_y)^{1/2}$]. As shown in the inset of

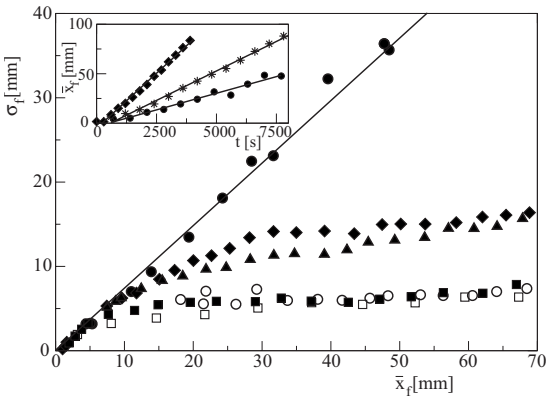

FIG. 7. Variation of the fronts width σ_f as a function of the mean front position $\overline{x_f}$. Empty symbols stand for stable configurations and filled symbols for unstable ones. Squares, triangles, diamonds, and circles correspond to $|N_g|=0.001\,25$, 0.02, 0.04, and 0.2, respectively. Inset: Variation of $\overline{x_f}$ as a function of time in the unstable configuration for $N_g=-0.2$ (●), $N_g=-0.08$ (*), and $N_g=-0.04$ (◆). Solid lines: Linear regressions on data points.

Fig. 7, the mean distance $\overline{x_f(t)}$ increases linearly with time even for the lowest flow velocity $N_g=-0.2$. The propagation of the isoconcentration fronts may therefore be characterized by the velocity $U_{c0.5}$ obtained by a linear regression on the variation of $\overline{x_f(t)}$ with t (□ and ■ symbols in Fig. 4). $U_{c0.5}$ is close to the flow velocity U (see Sec. III B) for $N_g \geqslant -0.08$; however, it is 40% higher at the lowest velocity ($N_g=-0.2$). This confirms other indications of a transition toward a different type of front growth dynamics (in this latter case, $U_{c0.5}$ is likely determined by the development of the few large fingers observed in Fig. 6).

The variation of σ_f with $\overline{x_f(t)}$ is displayed in Fig. 7. At the lowest flow rates (or largest $|N_g|$ values), the differences between the concentration maps of Figs. 1(a) and 1(d) are reflected in the variations of σ_f with $\overline{x_f}$. For $|N_g|=0.2$, σ_f increases roughly linearly with $\overline{x_f}$ in the unstable case [(●) symbols], while in the stable configuration, it quickly reaches a limit [(○) symbols]. At the highest velocity (i.e., $|N_g|=0.001\,25$), σ_f becomes constant and equal to 6 mm as soon as the distance from the injection line is larger than 10 mm. Its value is then the same in the stable and unstable flow configurations (■,□): This agrees with the comparison of Figs. 1(c) and 1(f) which do not display any difference due to buoyancy. At the intermediate velocities ($|N_g|=0.02-0.04$), the limiting value of σ_f is higher in the unstable configuration (▲,◆) than in the stable one and the distance $\overline{x_f}$ required to reach this limit is greater. In contrast, the variations observed in the stable case (open symbols) are nearly independent of the flow velocity.

This suggests that in the unstable configuration and in the range of N_g values ($-0.1 \leqslant N_g < -0.01$), two distinct regimes are successively observed. At short distances, the displacement is controlled by the instability while the variation of σ_f is similar to that measured for $N_g=-0.2$. At larger distances, σ_f levels off and becomes nearly constant like for stable displacements. The transition distance increases with N_g: For $N_g=-0.2$, it is of the order of the sample length, explaining why the second regime is not observed. Together with previous results, this observation allows one to estimate analytically the dispersivity for $N_g < N_g^c$.

In order to compare these results to those of Sec. III C, note that σ_f refers to the extension of the isoconcentration front $c=0.5$ in the flow direction: It does not include the influence of the width of the concentration profile (nonzero even at a given transverse distance y). At high velocities, for instance, the isoconcentration front is nearly flat [Fig. 6(a)] with only a few spikes. In this case, σ_f has a nonzero limit at long distances (due to these small features) and does not increase as $t^{0.5}$ like the width of the global profile $C(x,t)$ discussed in Sec. III C. In the unstable cases and at low velocities, the linear increase of σ_f at long distances reflects directly the buoyant rise of fingers: Its dynamics differs from that of the global spreading of the mixing zone. The latter combines several mechanisms (including, but not only, the growth of the fingers) leading to increase of the global width of the profile as $t^{0.5}$.

IV. ESTIMATION OF DISPERSIVITY VARIATIONS FOR UNSTABLE DISPLACEMENTS

The development of fingers driven by buoyancy forces in the unstable configuration is opposed by lateral mixing induced by transverse dispersion: The latter reduces the local density contrast δ_ρ between the fingers and the surrounding fluid and, finally, the buoyancy forces. As pointed out in Sec. III E, the structure of the displacement front has a characteristic size λ constant and close to 4 mm for gravity numbers in the range $-0.2 < N_g < -0.01$. The characteristic exchange time τ for lateral mixing will then be of the order of the transverse diffusion time across the half-width λ/2 with

$$\tau = \frac{\lambda^2}{8D_\perp}, \tag{5}$$

in which $D_\perp$ is the transverse dispersion coefficient.

The rising motion of the fingers driven by buoyancy forces should have a velocity u_{finger} proportional to the local density contrast $\delta\rho$ with $u_{\text{finger}} \sim (\delta\rho/\Delta\rho U_g)$. If the variation of $\delta\rho$ with time results solely from transverse mixing, then $\delta\rho$ will decrease exponentially with a time constant of the order of the transverse mixing time τ. This leads to $u_{\text{finger}} \sim U_g \exp(-t/\tau)$ and the vertical displacement $l(\tau)$ of the rising finger before its velocity goes to zero will be given by

$$l(\tau) \simeq \tau U_g. \tag{6}$$

$l(\tau)$ is then the typical spreading distance of the front due to buoyancy driven motions during the time τ: It should be of the order of the limiting value of the width σ_f of the isoconcentration lines at long distances. The transverse dispersion coefficient $D_\perp$ generally decreases with the Péclet number (or equivalently with the flow velocity U) so that both τ and $l(\tau)$ should increase at low velocities. This agrees with the observed increase of σ_f at long distances. At very low velocities, $l(\tau)$ reaches (or exceeds) the system size as observed for $N_g=-0.2$: In that case, σ_f keeps increasing with distance and does not reach a constant value within the model length.

The dispersion coefficient component $l_{d\ \text{buoyancy}}$ resulting from these buoyancy driven motions may be estimated by assuming that τ is the characteristic crossover time toward diffusive front spreading: The corresponding width $l(\tau)$ should then verify $l(\tau)^2 \simeq 2D_{\text{buoyancy}}\tau$. Combining with Eqs. (5) and (6) leads to the following dispersivity component $l_{d\ \text{buoyancy}} = D_{\text{buoyancy}}/U$:

$$l_{d\ \text{buoyancy}} = \frac{U_g^2 \lambda^2}{16 U D_\perp}. \tag{7}$$

The total dispersivity l_d is now taken to be equal to the sum of the dispersivity l_d^{eq} for a fully passive tracer and of $l_{d\ \text{buoyancy}}$ which assumes that these two processes are independent: This is only an approximation since the spatial flow velocity variations in the model influence both spreading processes.

The normalized passive tracer dispersivity l_d^{eq}/a may be estimated from data obtained with the polymer solutions for which, as noted above, no buoyancy effect is visible. The equation

$$\frac{l_d^{\text{eq}}}{a} \simeq f \text{Pe}^{\alpha}, \tag{8}$$

where $\alpha = 0.35 \pm 0.03$ and $f = 1.5 \pm 0.3$, has been selected for that purpose: It provides indeed a good global fit (dashed line in Fig. 5) with the polymer data at all Pe values and an acceptable one with water-glycerol data either in the stable configuration or at high velocities.

Combining Eqs. (7) and (8) and replacing U by its expression as a function of Pe leads then to

$$\frac{l_d}{a} = f \text{Pe}^{\alpha} + \frac{U_g^2 \lambda^2}{16 \epsilon \text{Pe}^{1+\beta_T} D_m^2}, \tag{9}$$

in which ϵ is a constant. In this equation, the transverse dispersion coefficient $D_\perp$ is assumed to vary as $D_\perp = D_m e \text{Pe}^{\beta_T}$, as suggested by numerical simulations from Ref. 20 for networks of capillaries of random radii.

In order to put more emphasis on the buoyancy controlled regime at low flow velocities (low Pe), the variation of the dispersivity is plotted in Fig. 8 as a function of 1/Pe. For unstable flows, as soon as $1/\text{Pe} > 0.0025 (1/400)$, l_d steadily increases with 1/Pe. This is also the case of the buoyancy component estimated by subtracting the passive tracer dispersivity component l_d^{eq} from the values of l_d. The difference $l_d - l_d^{\text{eq}}$ increases linearly with 1/Pe and can be fitted by the second term of Eq. (9) with $\epsilon = 0.3$ and $\beta_T \simeq 0$ (continuous line in the inset of Fig. 8).

The experimental value of β_T is lower than that reported in Ref. 20 ($\beta_T = 0.2$); this latter result corresponds to numerical simulations for capillary tube networks with a normalized standard deviation σ_a/a of the channel aperture equal to ours ($\sigma_a/a = 0.3$). However, in our experiments, the influence of the $l_{d\ \text{buoyancy}}$ term is mostly significant at the lower Péclet numbers ($\text{Pe} \leqslant 50$), while the simulations of Ref. 20 deal with $\text{Pe} \geqslant 300$. The variation of $D_\perp$ for $\text{Pe} \leqslant 50$ may therefore be expected to be slower (and the corresponding exponent lower) due to the influence of the molecular diffusion coefficient D_m which is a constant lower limit at very low Pe values.

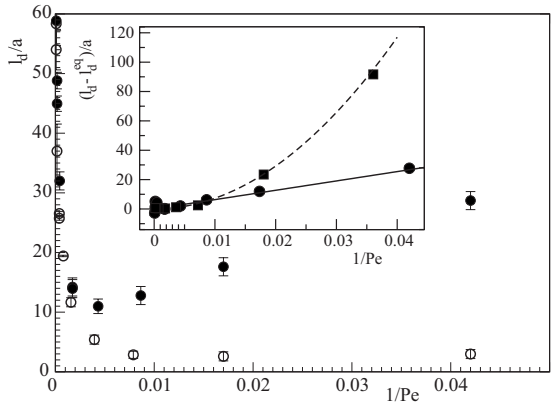

FIG. 8. Variation of l_d/a as function of $1/\text{Pe}$ for the water-glycerol solution. The filled circles correspond to $N_g < 0$ and empty circles to $N_g > 0$. Inset: Variation of $(l_d - l_d^{\text{eq}})/a$ as a function of $1/\text{Pe}$ for unstable experiments in a 2D network (●) and a 3D porous medium (■) (Ref. 5). In order to make comparisons easier, horizontal coordinates for the 3D data points have been divided by a factor of 5 and vertical coordinates by 0.6. Regressions corresponding to power laws of exponents of 1 (solid lines) and 2.1 (dotted lines) are superimposed on the data.

In the present work, the variation of the coefficient of dispersion D results directly from the 2D nature of the network which has been used. In a 3D porous medium, a bead packing, for instance, D depend weakly on the Péclet number.[2,5,8] In this case, α ranges between 0 and 0.2 and β_T between 1 and 1.2.[3] As a result, the difference $l_d - l_d^{\text{eq}}$ estimated from the model is expected to increase with Pe like $\simeq 1/\text{Pe}^2$. We have tested this prediction by reanalyzing the dispersion coefficients measured by Freytes *et al.*[5] In this work, gravity driven instabilities were studied in a model porous packing of 1 mm glass beads and for a density difference $\Delta\rho = 10^{-3}$ g/l. For water and in the high Pe regime where the effect of buoyancy is negligible, their data show that $l_d^{\text{eq}} \propto \text{Pe}^{0.1 \pm 0.1}$, indicating that $\beta_T \simeq 1.1 \pm 0.1$. As above, the buoyancy component is estimated by subtracting the passive tracer dispersivity l_d^{eq} from the measured dispersivities. The difference $l_d - l_d^{\text{eq}}$ obtained in this way varies as $(1/\text{Pe})^{1.9 \pm 0.2}$ (see inset of Fig. 8) with an exponent of 1.9 close to the value $1 + \beta_T \simeq 2.1 \pm 0.1$ predicted by the model.

V. CONCLUSIONS

To conclude, the miscible vertical displacement measurements on transparent networks of channels reported here provide information on the mixing front of two miscible fluids of slightly different densities at both the local and macroscopic scales. Qualitatively, the macroscopic dispersion measurements obtained confirm previous ones performed on 3D porous media:[8] The key feature of this work is that additional new information is provided by the high resolution visualization of front structures of different sizes down to the

scale of individual channels. Using this information, front distortions resulting from instabilities in unstable density contrast configurations could be analyzed quantitatively.

In these systems, the global spreading of the front results from the combination of the effects of the disordered spatial variations of the velocity field (the only mechanism active in the passive tracer case) and of buoyancy driven flows; the latter may either decrease or reduce the dispersion depending on the gravitationally stable or unstable configuration of the fluids. For large Péclet numbers ($\mathrm{Pe} > 500$) (i.e., small gravity numbers $|N_g| < 0.01$), the displacement fronts are very similar in both configurations and the global shape of the isoconcentration fronts is flat. In this case, the front spreading characteristics and the dispersivity values are similar to those measured for shear-thinning polymer solutions.

In the stable configuration, the dispersivity decreases significantly for $\mathrm{Pe} < 500$ and becomes constant and close to 1 mm when $\mathrm{Pe} < 100$. At the same time, the geometry of the isoconcentration front is only weakly affected by the stabilizing effect of buoyancy.

In the unstable configuration and at moderate N_g values (e.g., $-0.2 < N_g < -0.01$), the initial development of the instabilities is damped by transverse hydrodynamic dispersion after some time. As a result, front spreading remains dispersive but with a dispersivity increasing at low velocities as $l_d \simeq 1/\mathrm{Pe}$. These instability fingers are reflected in the geometry of the isoconcentration fronts which display large spikes and troughs. In this range of N_g values, the location (in the transverse direction) and the width of the spikes are observed to be constant. The spreading in the flow direction as a function of time displays two regimes: Initially (short distances from the injection), the width of the isoconcentration fronts increases linearly and then it levels off toward a constant value at larger distances.

In order to explain these results, an approach combining the influences of longitudinal buoyancy forces parallel to the mean flow and of the exchange of solute between the instability fingers and the surrounding fluid has been developed: It accounts semiquantitatively for the dependence of the dispersivity on the Péclet number if $N_g > -0.2$. The present observations on 2D networks and previous measurements on 3D bead packings (for which $l_d \simeq 1/\mathrm{Pe}^2$) are well fitted by this model.

At the lowest velocity investigated ($N_g = -0.2$), large fingers develop on the interface; the concentration front is strongly distorted but its spreading is still dispersive. Yet, the number of fingers on the isoconcentration front decreases with time while its width parallel to the flow keeps increasing with distance. This suggests that, at lower negative N_g values, gravitational instabilities might control the transport process. In 3D porous media, a linear growth of the mixing zone reflecting the dominant influence of such instabilities is only observed for N_g lower than a threshold value $N_g \simeq -1.5$.[7]

Further studies are needed to confirm our observation by using pairs of fluids with different density contrasts. Another issue of practical interest is the influence of the viscosity contrast on the spatial distribution of the tracer.

ACKNOWLEDGMENTS

We thank C. Zarcone and the "Institut de Mécanique des Fluides de Toulouse" for realizing and providing us with the micromodel used in these experiments and G. Chauvin and R. Pidoux for realizing the experimental setup. This work has been realized in the framework of ECOS Sud Program No. A03-E02 and of CNRS-CONICET Franco–Argentinian "Programme International de Cooperation Scientifique" (PICS No. 2178). M. V. D'Angelo has been supported by a fellowship of the University of Buenos-Aires.

[1] J. Bear, *Dynamics of Fluids in Porous Media* (Elsevier, New York, 1972).
[2] F. A. L. Dullien, *Porous Media, Fluid Transport and Pore Structure*, 2nd ed. (Academic, New York, 1991).
[3] M. Sahimi, *Flow and Transport in Porous Media and Fractured Rock* (VCH, Weinheim, 1995), Chap. 12.
[4] E. Charlaix, J. P. Hulin, C. Leroy, and C. Zarcone, "Experimental study of tracer dispersion in flow through two-dimensional networks of etched capillaries," J. Phys. D **21**, 1727 (1988).
[5] M. A. Freytes, A. d'Onofrio, M. Rosen, C. Allain, and J. P. Hulin, "Gravity driven instabilities in miscible non-Newtonian fluid displacements in porous media," Physica A **290**, 286 (2001).
[6] C. Oltean, Ch. Felder, M. Panfilov, and M. A. Bués, "Transport with a very low density contrast in HeleShaw cell and porous medium: Evolution of the mixing zone," Transp. Porous Media **55**, 339 (2004).
[7] T. Menand and A. W. Woods, "Dispersion, scale, and time dependence of mixing zones under gravitationally stable and unstable displacements in porous media," Water Resour. Res. **41**, W05014 (2005).
[8] T. C. Flowers and J. R. Hunt, "Viscous and gravitational contributions to mixing during vertical brine transport in water-saturated porous media," Water Resour. Res. **43**, W01407 (2007).
[9] R. A. Schincariol, F. W. Schwartz, and C. A. Mendoza, "Instabilities in variable density flows: Stability and sensitivity analyses for homogeneous and heterogeneous media," Water Resour. Res. **33**, 31 (1997).
[10] M. Beinhorn, P. Dietrich, and O. Kolditz, "3-D numerical evaluation of density effects on tracer tests," J. Contam. Hydrol. **81**, 89 (2005).
[11] K. Johannsen, S. Oswald, R. Held, and W. Kinzelbach, "Numerical simulation of saltwater-freshwater fingering instabilities observed in a porous medium," Adv. Water Resour. **29**, 1690 (2006).
[12] R. Lenormand, C. Zarcone, and A. Sarr, "Mechanism of the displacement of one fluid by another in a network of capillary ducts," J. Fluid Mech. **135**, 337 (1983).
[13] M. V. D'Angelo, H. Auradou, C. Allain, and J.-P. Hulin, "Pore scale mixing and macroscopic solute dispersion regimes in polymer flows inside two-dimensional model networks," Phys. Fluids **19**, 033103 (2007).
[14] *Experimental Methods in the Physical Sciences*, edited by P. Z. Wong (Academic, London, 1999), Vol. 35.
[15] V. Kretz, P. Berest, J. P. Hulin, and D. Salin, "An experimental study of the effects of density and viscosity contrasts on macrodispersion in porous media," Water Resour. Res. **39**, 1032 (2003).
[16] S. Tenchine and Ph. Gouze, "Density contrast effects on tracer dispersion in variable aperture fractures," Adv. Water Resour. **28**, 273 (2005).
[17] *Conn's Biological Stains: A Handbook of Dyes, Stains and Fluorochromes for Use in Biology and Medicine*, edited by R. W. Horobin and J. A. Kiernan (BIOS Scientific, Oxford, 2002).
[18] A. Boschan, H. Auradou, I. Ippolito, R. Chertcoff, and J. P. Hulin, "Miscible displacement fronts of shear thinning fluids inside rough fractures," Water Resour. Res. **43**, W03438 (2007).
[19] R. A. Wooding, "Growth of fingers at an unstable diffusing interface in a porous medium or Hele-Shaw cell," J. Fluid Mech. **39**, 477 (1969).
[20] C. Bruderer and Y. Bernabé, "Network modeling of dispersion: transition from Taylor dispersion in homogeneous networks to mechanical dispersion in very heterogeneous ones," Water Resour. Res. **37**, 897 (2001).